ARTICLES
https://doi.org/10.1038/s41561-018-0225-2
nature geoscience

Slab stagnation due to a reduced viscosity layer beneath the mantle transition zone

Wei Mao* and Shijie Zhong*

The linear structures of seismically fast anomalies, often interpreted as subducted slabs, in the southern Asia and circum-Pacific lower mantle provided strong evidence for the whole mantle convection model. However, recent seismic studies have consistently shown that subducted slabs are deflected horizontally for large distances in mantle transition zone in the western Pacific and other subduction zones, suggesting that the slabs meet significant resistance to their descending motion and become stagnant in the transition zone. This poses challenges to the whole mantle convection model and also brings the origin of stagnant slabs into question. Here, using a global mantle convection model with realistic spine–post-spinel phase change (−2 MPa K^{-1} Clapeyron slope) and plate motion history, we demonstrate that the observed stagnant slabs in the transition zone and other slab structures in the lower mantle can be explained by the presence of a thin, weak layer at the phase change boundary that was suggested by mineral physics and geoid modelling studies. Our study also shows that the stagnant slabs mostly result from subduction in the past 20–30 million years, confirming the transient nature of slab stagnation and phase change dynamics on timescales of tens of millions of years from previous studies.

The whole mantle model was established in 1990s on the basis of seismic observations of subducted slabs in the lower mantle[1–3] and was supported by whole mantle convection models that reproduce the general seismic slab structure in the lower mantle[4–6] and the long-wavelength geoid[4,7,8]. However, recent seismic observations of ubiquitous slab stagnation in the transition zone in many subduction zones[9–13] (Fig. 1a–c, Fig. 2a,b, Supplementary Figs. 1 and 2 and Supplementary discussion) have presented new challenges to the whole mantle model. The best example of stagnant slabs in the transition zone is in the northern Honshu subduction zone, where the slab extends horizontally for >1,500 km beneath East Asia (Fig. 2a). These stagnant slabs are suggested to be responsible for tectonism and volcanism in overriding continental regions (for example, in Northeast China)[13,14]. Some studies also suggested stagnant slabs at ~1,000 km depth[12], but there seems to be less agreement about the depth extent of these lower mantle slabs among different studies[15] (Supplementary Fig. 1 and 2 and Supplementary discussion).

The cause of stagnant slabs in the transition zone has been extensively studied[15–18], but large uncertainties remain. Previous mantle convection studies suggest that the endothermic spinel–post-spinel phase change[19–21], trench retreat[16–18,22,23], the viscosity increase with depth[24,25], slab viscosity[26–28] and non-equilibrium pyroxene garnet transition[29] may have significant effects on slab dynamics at around 670 km depth. However, because these studies were conducted in two-dimensional (2D) models, it is difficult to apply them to interpret seismic slab structures. Another significant challenge comes from recently reported Clapeyron slopes of −0.4 to −2.5 MPa K^{-1} for the phase change from mineral physics[30–32] and seismic studies[11] that are significantly smaller than that suggested for producing stagnant slabs in many 2D convection models[16,17,23], although some other studies reported smaller threshold Clapeyron slopes[18].

Mantle convection model set-up

We have formulated 3D spherical models of mantle convection with plate motion and trench retreat history[33], depth- and temperature-dependent viscosity, and the spinel–post-spinel phase change (see Methods) with the goal of understanding the origin of stagnant slabs and other slab structures. In this study, we only consider the phase change at 670 km depth from spinel to post-spinel phases (Supplementary Table 1). We use plate motion history[33] as a time-dependent surface velocity boundary condition, whereas the core–mantle boundary (CMB) is free-slip. The models are computed for the past 130 million years (Myr) (see Methods). The surface temperature is prescribed as a constant 0, whereas the CMB is thermally insulating. The insulating CMB prohibits the formation of upwelling plumes, to allow our models to concentrate on the evolution of subducted slabs. Given that subducted slabs are much more important energy transfer agents than upwelling plumes in the top 2,000 km of the mantle[34], the exclusion of mantle upwelling plumes in our models is justified. The initial mantle non-dimensional temperature below the lithosphere is 0.52 (or 1,300 °C) (that is, from 150 km depth to the CMB), whereas the initial lithospheric temperature is calculated from a cooling plate model[35] using oceanic crust ages at 130 Myr ago[36] (Ma) (see Methods). Our models are similar to previous studies[6,37,38] except that we include the phase change, insulating CMB or different plate motion models.

Our models use a temperature- and depth-dependent viscosity (Methods). The viscosity pre-factor for depths ranging from 150 km to 670 km is reduced by a factor of 100 to produce a relatively strong lithosphere and lower mantle[7,8]. Some cases also consider a thin, weak layer below the spinel–post-spinel phase boundary to simulate the rheological effects of the phase change due to grain-size reduction and superplasticity[39,40] that has been shown to be consistent with the geoid models[8]. The activation energy is chosen such that the viscosity varies by four orders of magnitude for temperatures ranging from 0 to 1.

With the prescribed plate motions as boundary conditions, trench motions in our models are not dynamically determined, differing from fully dynamic models that by employing either faulted plate boundary[16] or highly nonlinear rheology[18,23,25,41–43] produce dynamic trench and plate motions. The prescribed trench motions may affect slab interaction with the transition zone, compared with

Department of Physics, University of Colorado, Boulder, CO, USA. *e-mail: wei.mao@colorado.edu; szhong@colorado.edu

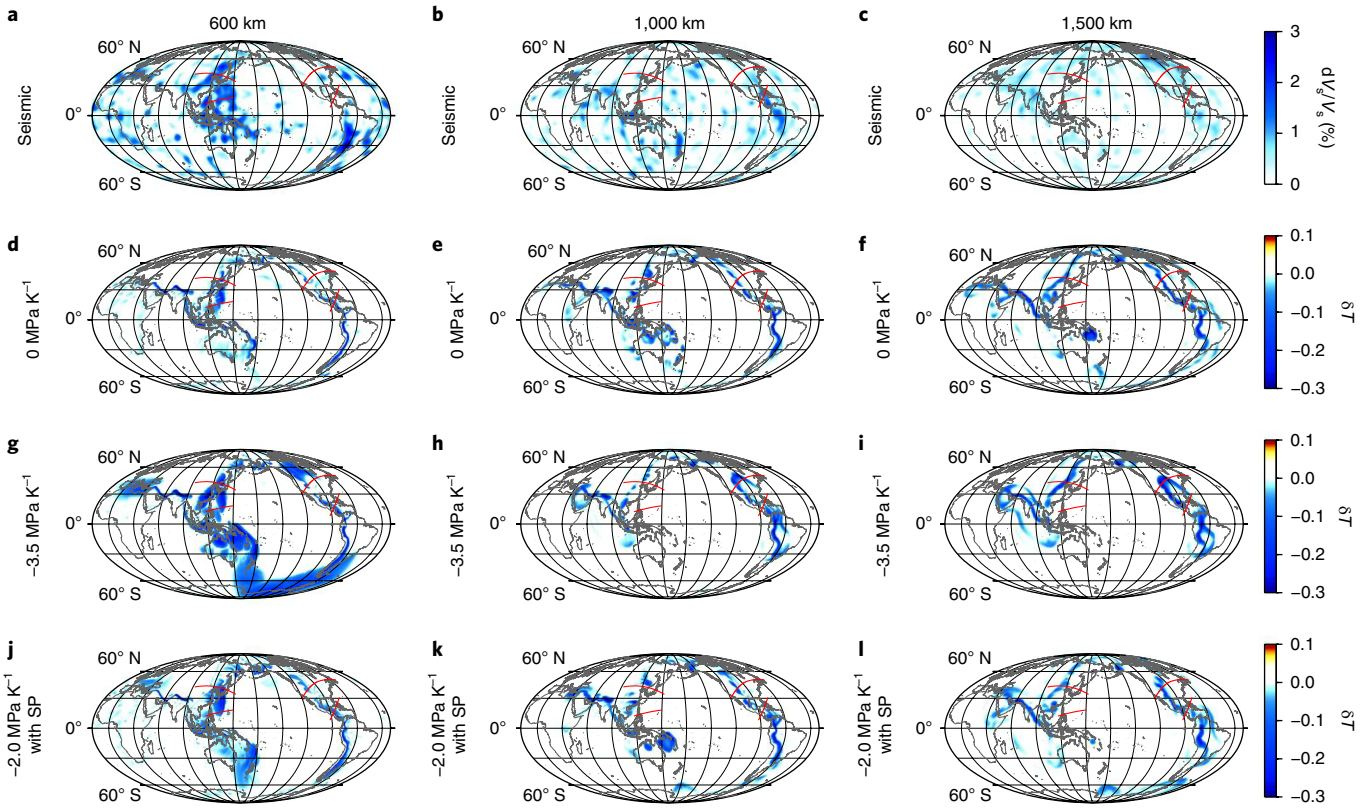

Fig. 1 | Map view of seismic anomalies and present-day model temperature anomalies. a–c, Shear-wave velocity (V_s) anomalies at 600, 1,000 and 1,500 km depths from seismic model SEMUCB_WM1[10], respectively (only showing positive anomalies to highlight the slabs). **d–l**, Present-day dimensionless temperature anomalies at the three depths for Cases 1 (**d–f**), 3 (**g–i**) and 4 (**j–l**), respectively. Temperature anomalies $\delta T = T - T_{ave}(r)$, where $T_{ave}(r)$ is the horizontally averaged temperature at radius r. In **j–l**, SP represents superplasticity. In each figure, the four red lines represent cross-sections for the northern Honshu, northern Mariana, North America and Central America subduction zones that were used in ref. [12].

fully dynamic trench motions. However, given the uncertainty and complexity of lithospheric rheology[44,45], it is difficult for currently available fully dynamic models to reproduce the observed trench and plate motion history that is needed to interpret seismic slab structures. Furthermore, the lower mantle viscosity in our models is ~2.5×10^{22} Pa s (Methods and Supplementary Fig. 3b), similar to that inferred from the post-glacial rebound studies[8], suggesting that the imposed plate motions are compatible with the Rayleigh number in our models.

Slab structures from conventional convection models

We first present Case 1, which does not have any phase change (Supplementary Table 1). Case 1 shows that after 130 Myr of model integration to the present day, the slabs in most subduction zones (for example, Japan, Tethys and the Americas) penetrate through the 670 km depth into the lower mantle to the CMB (Figs. 1d–f, 2e–h, and Supplementary Fig. 4e–h and 5b). However, in the Bonin-Mariana subduction zone, the slabs are deflected horizontally in the transition zone and also show double-slab structure (Figs. 1d, 2f), whereas Tonga slabs are mostly limited above ~1,500 km depth (Supplementary Fig. 4e). These slab structures result from unique characteristics of plate motion history, including substantial trench retreat for the past 50 Myr at the Mariana (Fig. 3a) and relatively short duration of subduction at the Tonga subduction zone. In the northern Honshu subduction zone, the slab has a shallow dip angle but does not show slab stagnation in the transition zone (Fig. 2e). The Honshu slab ends at ~1,000 km depth with a significant gap from the lower mantle slabs that may result from slab detachment associated with the subduction of young lithosphere around 55 Ma (Fig. 3b).

Compared with seismic structure (Figs. 1a–f, 2a–h, Supplementary Figs. 4a–h and 5a,b), the largest difference occurs in the transition zone where Case 1 fails to reproduce stagnant slabs in the Honshu, Tonga and Calabria (the southern Europe) subduction zones. The lower mantle slabs, on the other hand, are generally consistent with the seismic model, including the Farallon and Tethys slabs, and slabs in eastern Asia, Central and South America, but significant differences exist for small-scale features. The model Farallon slab appears significantly more westward than in the seismic model, a feature that is also evident in previous models[46] and may require more sophisticated modelling of lithosphere–mantle coupling[47]. It should be pointed out that the slabs from Case 1 should be similar to those in previous models[37,38], although those models focused on long-wavelength mantle structure or mantle plumes.

Cases 2 and 3 include the spinel–post-spinel phase change with Clapeyron slopes γ of -2 MPa K^{-1} and -3.5 MPa K^{-1}, respectively, but are otherwise identical to Case 1. Case 2 displays very similar slab structures to Case 1 with no significant slab stagnation in the transition zone (Supplementary Fig. 6), whereas Case 3 with a large γ (-3.5 MPa K^{-1}) shows widespread slab stagnations in the southern Pacific and southern Europe, where the slabs are largely stopped in the transition zone and are absent in the lower mantle (Fig. 1g–i and Supplementary Figs. 4i, 4k, 5c). The widespread stagnant slabs in the transition zone found in the southern Pacific at the present day in Case 3 result from horizontal spreading of subducted slabs associated with the subduction of the Catequil plate under Antarctica from 120 to 100 Ma[33] (Supplementary Fig. 7a–d), but are inconsistent with the seismic models (Fig. 1a). However, the slab structures in both the upper and lower mantle

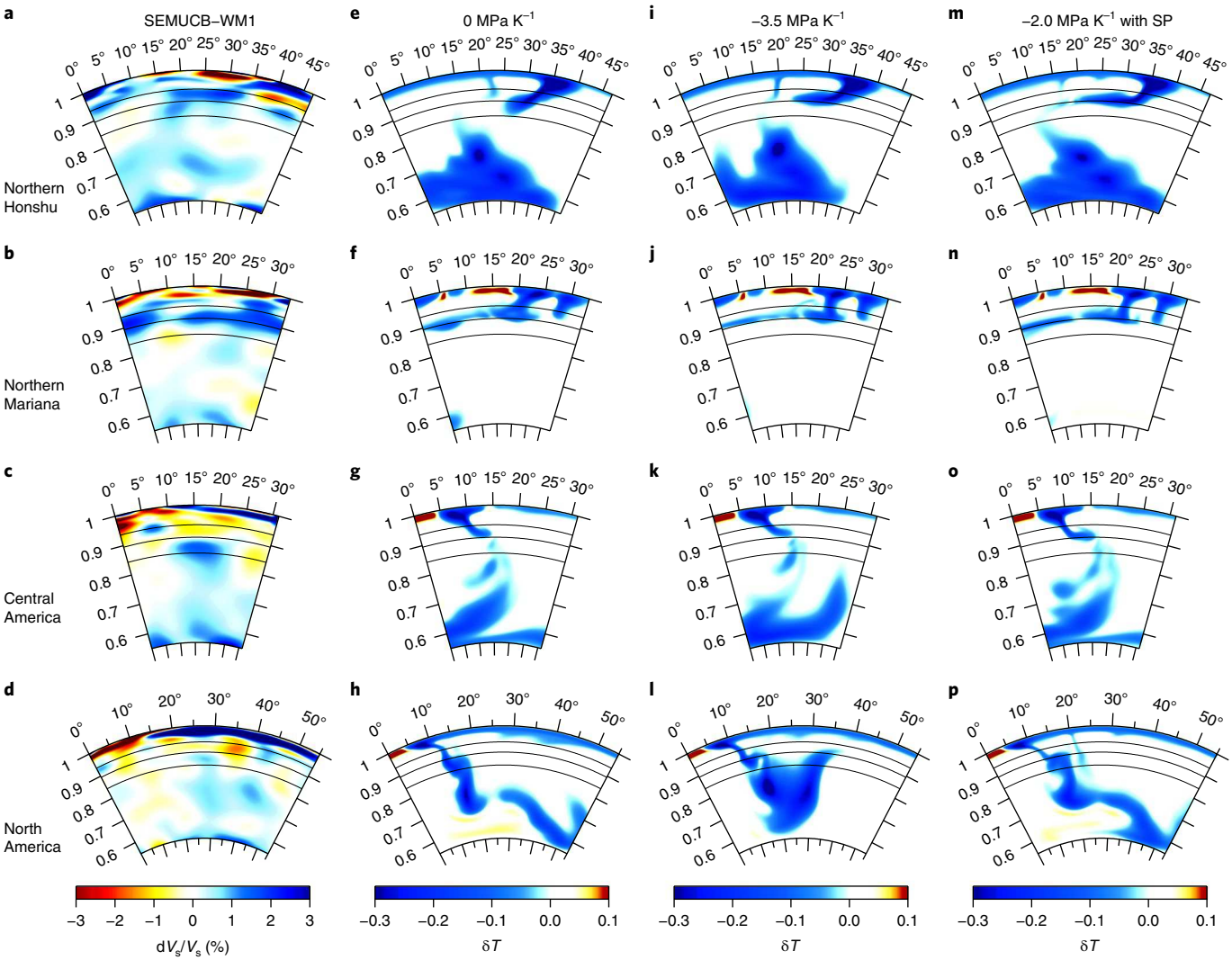

Fig. 2 | Cross-sectional view of seismic anomalies and present-day model temperature anomalies for subduction zones. The four rows are for the northern Honshu, northern Mariana, Central America and North America subduction zones, respectively. **a**–**d**, Shear wave velocity anomalies for these four subduction zones from model SEMUCB_WM1[10]. **e**–**p**, Model dimensionless temperature anomalies for these four subduction zones marked in Fig. 1 for Cases 1 (**e**–**h**), 3 (**i**–**l**) and 4 (**m**–**p**), respectively. These cross-sections are made along great circles, and the vertical axis is dimensionless radius r. The three lines correspond to 410 km, 670 km and 1,000 km depths, respectively.

from Case 3 are remarkably similar to those in Cases 1 and 2 in eastern Asia, the western Pacific, western Java, the Americas and Tethys subduction zones (Figs. 1, 2e–l, Supplementary Figs. 4e–l and 6), although Cases 1–3 use very different values of γ. In eastern Asia (including the Honshu), the slabs from Case 3 show moderate stagnation in the transition zone but much less than that found in the seismic models (Fig. 2a,i). In the Americas, the large γ in Case 3 does not lead to any slab stagnation in the transition zone (Fig. 2k,l and Supplementary Fig. 4j).

Cases 1–3 demonstrate that although the main seismic structures of lower mantle slabs in the Americas, eastern Asia and Tethys can be reproduced in convection models with plate motion history[4–6], the stagnant slabs in the transition zone, especially in the Japanese subduction zone, represent a challenge for these convection models even with an unrealistically large γ of $-3.5\,\mathrm{MPa\,K^{-1}}$ (as in Case 3). Case 3 also suggests that the effect of the phase change on slab structure is not the same for all subduction zones, and demonstrates the necessity of formulating 3D global convection models with realistic plate motion histories (such as that used in this study) to interpret the seismic observations.

Controls on slab stagnation in the transition zone

Case 4 employs a smaller but realistic value of γ ($-2\,\mathrm{MPa\,K^{-1}}$) and a thin weak layer at the base of the transition zone as suggested by other geophysical investigations[8,39,40]. The weak layer promotes the formation of stagnant slabs in the transition zone, thus helping to explain the seismic slab structures, especially in the Northern Honshu and Calabria subduction zones (Figs. 1j,2m, Supplementary Fig. 4o). For the northern Honshu subduction zone, because the weak layer reduces resistance to horizontal spreading of slabs above the phase-change boundary, the deflected slab in the transition zone extends much further westwards under the northeast China, similar to the seismic models (Fig. 2a,m). However, the weak layer does not prevent the Antarctica-Catequil slabs from going into the lower mantle, thus agreeing with the seismic models—unlike Case 3 with $\gamma = -3.5\,\mathrm{MPa\,K^{-1}}$ (Fig. 1, Supplementary Figs. 5 and 7). Stagnant slabs in the transition zone in the Bonin-Mariana, Tonga, Calabria and Western Java subduction zones are also largely reproduced in Case 4 (Fig. 2 and Supplementary Fig. 4). The model slabs descend to the lower mantle, and even the CMB in the Honshu and Americas subduction zones, similar to Cases 1 and 2 and the seismic models.

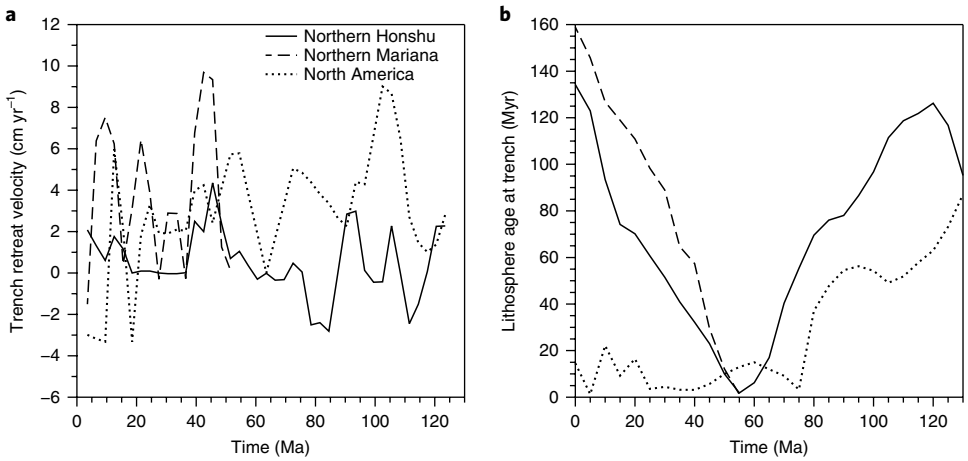

Fig. 3 | Trench migration and age of subducting lithosphere at different subduction zones. a,**b**, Time-dependent trench motion (**a**) and age of subducting lithosphere at trench (**b**) for the northern Honshu, northern Mariana and North America subduction zones. Positive values indicate trench retreat, whereas negative values represent trench advance (see Methods). Mariana trench motion covers only the past 50 Myr since trench creation. The minimum age for subducting lithosphere for the northern Honshu subduction zone at 55 Ma reflects the subduction of the mid-ocean ridge of the Izanagi plate.

The Tonga, Calabria and Western Java slabs, although deflected in the transition zone, also descend into the lower mantle in agreement with the seismic models (Supplementary Fig. 2 and 4).

A comparison of slab evolution with surface plate motion history suggests that trench retreat exerts a significant control on slab deflection above 670 km depth, consistent with previous studies[15–18,22,23]. The ~1,500-km-long horizontally deflected slab in the transition zone of the Northern Honshu subduction zone in Case 4 has developed only in the past 20 Myr (Fig. 4d–f and Supplementary Fig. 7h) during the opening of Japan Sea, when the trench retreated at a rate of approximately 1.5 cm yr^{-1}(Fig. 3a)[48]. The Japanese trench had periods of trench advance and retreat over the past 120 Myr (Fig. 3a). At around 112 Ma, shortly after the model was initiated, the slab was deflected in the transition zone (Fig. 4a) due to the initial stage of trench retreat. By around 69 Ma, with the trench having moved back and forth, the slab descended into the lower mantle with no stagnant slab in the transition zone (Fig. 4b). Following a period of trench retreat from 60 to 40 Ma, the slab seems to accumulate in the transition zone again (Fig. 4c). The Farallon slab has experienced a similar structure evolution in relation to trench motion. During trench retreat from 130 to 20 Ma following the opening of Atlantic Ocean (Fig. 3a), the Farallon slab is trapped in the transition zone for approximately 30–40 Myr (Fig. 4g,h) before it descended into the lower mantle (Fig. 4i). As the trench retreat continued, the upper mantle slab accumulated in the transition zone, while the lower mantle slab continued its descent (Fig. 4j,k). With no steady trench retreat for the past 20 Myr, the slab readily entered the lower mantle (Fig. 4l).

It should be noted that when trench retreat is rapid as in the Mariana for the past 50 Myr (Fig. 3a), slab stagnation may occur in the transition zone above the high-viscosity lower mantle without the phase change, as in Case 1 (Fig. 2f). Whereas young, and hence warm, subducting lithosphere leads to a thin slab in the upper mantle, the effect of lithospheric age on slab stagnation is not as obvious (Figs. 3b and 4). The stagnant slabs seen at present for the Northern Mariana and Honshu subduction zones and at 90 Ma for the Farallon subduction zone in Case 4 are all associated with relatively old subducting lithosphere (Fig. 3b), consistent with that from the 2D fully dynamic models[18,23]. However, the horizontally deflected Farallon slab at ~40 Ma in Case 4 is also associated with relatively young lithosphere. This may reflect the effect of 3D mantle flow or a possible limitation of the prescribed trench motions in our models.

Eight additional models were computed to examine the effects of the weak layer, γ, Rayleigh number Ra and radial viscosity contrast. Compared with Case 4, the weak layer in Case 5 is ten times stronger (that is, the weak layer and transition zone have the same viscosity), whereas the weak layer in Case 6 is three times weaker (Supplementary Table 2). The stagnant slab in the Honshu is shorter for Case 5 with its stronger weak layer, as expected (Fig. 2m, Supplementary Fig. 8a,d). However, it appears that the weak layer in Case 4 with a viscosity that is ten times smaller than the transition zone is optimal in reproducing stagnant slabs in the Honshu, Mariana and Calabria (Fig. 2m,n, and Supplementary Figs. 4o and 8a–f). Cases 7 and 8 with $\gamma = -1.7$ MPa K^{-1} show similar results to those in cases with $\gamma = -2.0$ MPa K^{-1} (Supplementary Fig. 8).

Ra and viscosity contrast affect flow velocity and convective vigour, and hence the distance that slabs can travel over a given time period. Cases 9 and 10 differ from Case 4 only in Ra, whereas Cases 11 and 12 differ from Case 4 by having different viscosity contrasts between the upper and lower mantles (Supplementary Table 2). Seismic slab structures in the northern Honshu, North America, Tonga and Calabria subduction zones are better explained in models with an averaged lower mantle viscosity of $<5\times10^{22}$ Pa s (that is, Ra $>2\times10^{7}$, Supplementary Fig. 9) and a viscosity increase from the upper to lower mantles that is ~100 times (Supplementary Fig. 10) as in Case 4. A smaller Ra (that is, a larger mantle viscosity) leads to a slower slab motion. Therefore, for Case 9 with Ra $=2\times10^{7}$, the stagnant slab in the Honshu is significantly shorter, and the Farallon and Calabria slabs do not sink as deep (Supplementary Fig. 9a–c) as in Case 4, with Ra $=5\times10^{7}$. There is also significantly less stagnant slab in the Java (Supplementary Fig. 9d). Case 10 has a larger Ra of 10^{8}, and slabs move faster and are thinner in general. However, compared with Case 4, the stagnant slabs in the Calabria and Java are significantly reduced (Supplementary Fig. 9g and 9h), which may be inconsistent with the seismic models. For Case 11, with a smaller viscosity contrast ($\beta = 30$) than Case 4, the stagnant slabs in the transition zone are much shorter (Supplementary Fig. 10a–d), and are inconsistent with the seismic models. For Case 12, with $\beta = 300$, the stagnant slabs spread more in the transition zone (Supplementary Fig. 10e–h), and at the Tonga subduction zone, the slab even spreads to the east side of the trench, which seems to be inconsistent with the seismic model. At Calabria, Cases 11 and 12 both show little slab stagnation in the transition zone. Finally, Case 4HR, which is identical to Case 4 except for a significantly higher resolution, shows that our results are adequately resolved (Supplementary Fig. 11).

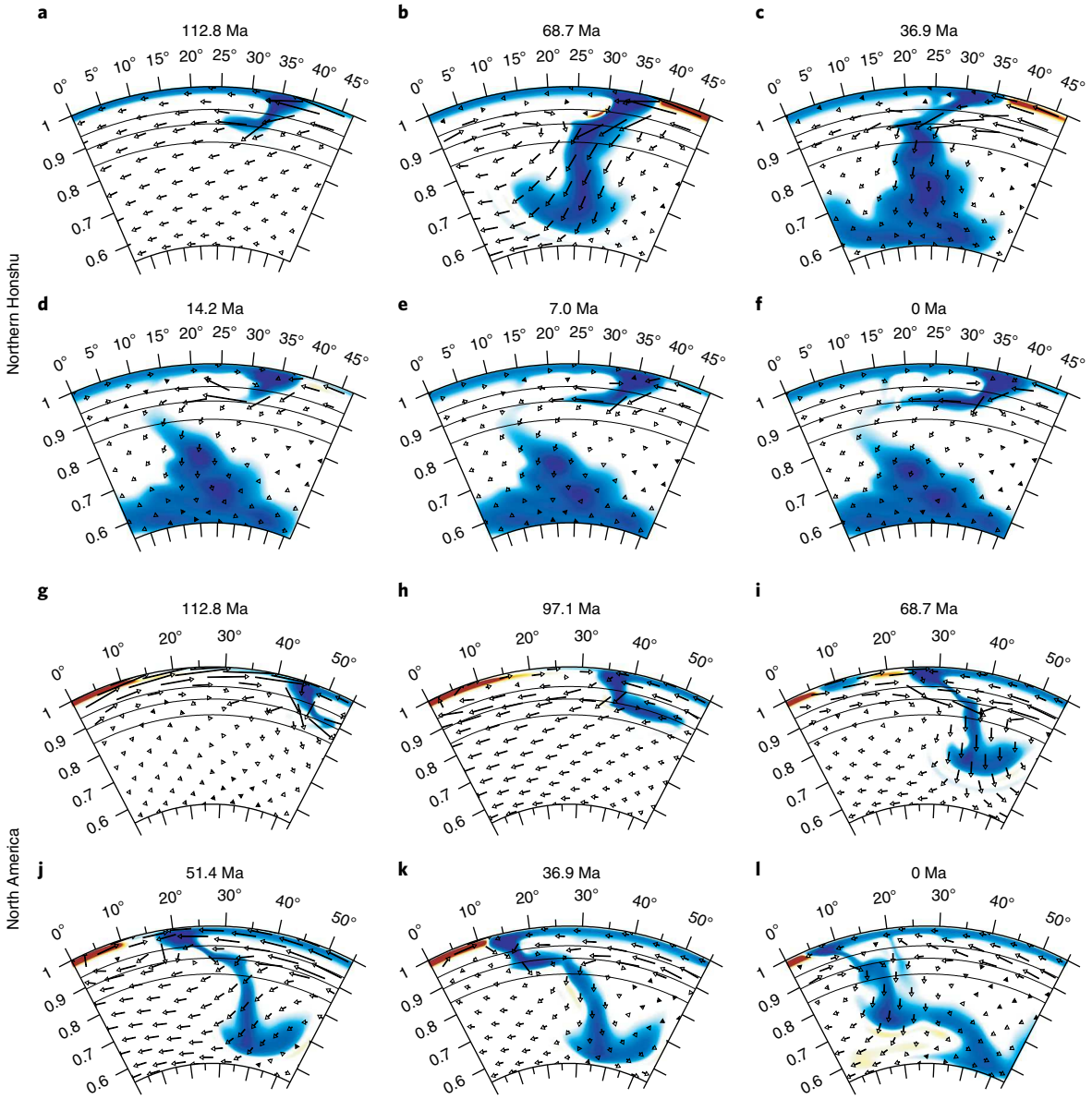

Fig. 4 | Cross-sectional view of the structure and flow velocity evolution for the northern Honshu and North America slabs from Case 4. a–f, Northern Honshu slab structure at 112.8, 68.7, 36.9, 14.2, 7.0 and 0 Ma, respectively. **g–l**, North America (Farallon) slab structure at 112.8, 97.1, 68.7, 51.4, 36.9 and 0 Ma, respectively. The arrows in each plot represent flow velocities that are parallel to the cross-sectional plane. The coloured scale bar for temperature anomaly is the same as that in Fig. 2.

Conclusions and implications for mantle dynamics

Our global mantle convection models with a realistic spinel–post-spinel phase change and plate motion history successfully explain the stagnant slabs in the transition zone and other slab structures in the lower mantle that are observed in seismic tomography studies. Our models demonstrate that the slabs interact with the phase change differently at different subduction zones, depending on 3D mantle flow and plate and trench motion histories, suggesting the necessity of formulating 3D global models with realistic plate motion histories to interpret seismic observations. Although a layer of reduced viscosity at the spinel–post-spinel phase change has been suggested previously based on mineral physics and geoid modelling[8,39,40], our modelling shows that this weak layer is key to producing stagnant slabs in the transition zone and other slab structures in the lower mantle—especially the large horizontal extent of stagnant slabs in the western Pacific. Consistent with previous studies[15–18,22,23], our models show that trench retreat plays an important role in causing slab stagnation in the transition zone. Our models indicate that stagnant slabs in the western Pacific subduction zones, including the Honshu and Mariana, have largely formed in the past 20–30 Myr. Our models also reveal the prevalent change in slab morphology between stagnation in the transition zone and penetration into the lower mantle on timescales of tens of millions of years, suggesting a transient nature of slab stagnation[15,16,49].

Online content

Any methods, additional references, Nature Research reporting summaries, source data, statements of data availability and associated accession codes are available at https://doi.org/10.1038/s41561-018-0225-2.

Received: 19 March 2018; Accepted: 9 August 2018;
Published online: 1 October 2018

References

1. Dziewonski, A. M. Mapping the lower mantle: determination of lateral heterogeneity in P velocity up to degree and order 6. *J. Geophys. Res. Solid Earth* **89**, 5929–5952 (1984).
2. Grand, S. P., van der Hilst, R. D. & Widiyantoro, S. Global tomography: a snapshot of convection in the Earth. *GSA Today* **7**, 1–7 (1997).
3. van der Hilst, R. D., Widiyantoro, S. & Engdahl, E. R. Evidence for deep mantle circulation from global tomography. *Nature* **386**, 578–584 (1997).
4. Ricard, Y., Richards, M. A., Lithgow-Bertelloni, C. & Le Stunff, Y. A geodynamic model of mantle density heterogeneity. *J. Geophys. Res.* **98**, 21895–21909 (1993).
5. Lithgow-Bertelloni, C. & Richards, M. A. The dynamics of Cenozoic and Mesozoic plate motions. *Rev. Geophys.* **36**, 27–78 (1998).
6. Bunge, H. P. et al. Time scales and heterogeneous structure in geodynamic Earth models. *Science* **280**, 91–95 (1998).
7. Hager, B. H. & Richards, M. A. Long-wavelength variations in Earth's geoid: physical models and dynamical implications. *Phil. Trans. R. Soc. Lond. A* **328**, 309–327 (1989).
8. Mitrovica, J. X. & Forte, A. M. A new inference of mantle viscosity based upon joint inversion of convection and glacial isostatic adjustment data. *Earth. Planet. Sci. Lett.* **225**, 177–189 (2004).
9. Ritsema, J., Deuss, A., Van Heijst, H. J. & Woodhouse, J. H. S40RTS: a degree-40 shear-velocity model for the mantle from new Rayleigh wave dispersion, teleseismic traveltime and normal-mode splitting function measurements. *Geophys. J. Int.* **184**, 1223–1236 (2011).
10. French, S. W. & Romanowicz, B. A. Broad plumes rooted at the base of the Earth's mantle beneath major hotspots. *Nature* **525**, 95–99 (2015).
11. Fukao, Y., Obayashi, M. Nakakuki, T. & Deep Slab Project Group. Stagnant slab: a review. *Annu. Rev. Earth. Planet. Sci.* **37**, 19–46 (2009).
12. Fukao, Y. & Obayashi, M. Subducted slabs stagnant above, penetrating through, and trapped below the 660 km discontinuity. *J. Geophys. Res. Solid Earth* **118**, 5920–5938 (2013).
13. Zhao, D., Tian, Y., Lei, J., Liu, L. & Zheng, S. Seismic image and origin of the Changbai intraplate volcano in East Asia: role of big mantle wedge above the stagnant Pacific slab. *Phys. Earth Planet. Inter.* **173**, 197–206 (2009).
14. Zou, H., Fan, Q. & Yao, Y. U–Th systematics of dispersed young volcanoes in NE China: asthenosphere upwelling caused by piling up and upward thickening of stagnant Pacific slab. *Chem. Geol.* **255**, 134–142 (2008).
15. Goes, S., Agrusta, R., Van Hunen, J. & Garel, F. Subduction-transition zone interaction: A review. *Geosphere* **13**, 644–664 (2017).
16. Zhong, S. J. & Gurnis, M. Mantle convection with plates and mobile, faulted plate margins. *Science* **267**, 838–843 (1995).
17. Christensen, U. R. The influence of trench migration on slab penetration into the lower mantle. *Earth. Planet. Sci. Lett.* **140**, 27–39 (1996).
18. Agrusta, R., Goes, S. & van Hunen, J. Subducting-slab transition-zone interaction: Stagnation, penetration and mode switches. *Earth. Planet. Sci. Lett.* **464**, 10–23 (2017).
19. Christensen, U. R. & Yuen, D. A. Layered convection induced by phase transitions. *J. Geophys. Res. Solid Earth* **90**, 10291–10300 (1985).
20. Tackley, P. J., Stevenson, D. J., Glatzmaier, G. A. & Schubert, G. Effects of an endothermic phase transition at 670 km depth in a spherical model of convection in the Earth's mantle. *Nature* **361**, 699–704 (1993).
21. Ita, J. & King, S. D. The influence of thermodynamic formulation on simulations of subduction zone geometry and history. *Geophys. Res. Lett.* **25**, 1463–1466 (1998).
22. van der Hilst, R. & Seno, T. Effects of relative plate motion on the deep structure and penetration depth of slabs below the Izu-Bonin and Mariana island arcs. *Earth. Planet. Sci. Lett.* **120**, 395–407 (1993).
23. Yang, T. et al. Cenozoic lithospheric deformation in Northeast Asia and the rapidly-aging Pacific Plate. *Earth. Planet. Sci. Lett.* **492**, 1–11 (2018).
24. Gurnis, M. & Hager, B. H. Controls of the structure of subducted slabs. *Nature* **335**, 317–321 (1988).
25. Garel, F. et al. Interaction of subducted slabs with the mantle transition-zone: a regime diagram from 2-D thermos-mechanical models with a mobile trench and an overriding plate. *Geochem. Geophys. Geosyst.* **15**, 1739–1765 (2014).
26. Zhong, S. J. & Gurnis, M. Role of plates and temperature-dependent viscosity in phase change dynamics. *J. Geophys. Res. Solid Earth* **99**, 15903–15917 (1994).
27. Čížková, H., van Hunen, J., van den Berg, A. P. & Vlaar, N. J. The influence of rheological weakening and yield stress on the interaction of slabs with the 670 km discontinuity. *Earth. Planet. Sci. Lett.* **199**, 447–457 (2002).
28. Billen, M. I. & Hirth, G. Rheologic controls on slab dynamics. *Geochem. Geophys. Geosyst.* **8**, Q08012 (2007).
29. King, S. D., Frost, D. J. & Rubie, D. C. Why cold slabs stagnate in the transition zone. *Geology* **43**, 231–234 (2015).
30. Katsura, T. et al. Post-spinel transition in Mg_2SiO_4 determined by high P–T in situ X-ray diffractometry. *Phys. Earth Planet. Inter.* **136**, 11–24 (2003).
31. Fei, Y. et al. Experimentally determined postspinel transformation boundary in Mg2SiO4 using MgO as an internal pressure standard and its geophysical implications. *J. Geophys. Res. Solid Earth* **109**, B02305 (2004).
32. Litasov, K. D., Ohtani, E., Sano, A., Suzuki, A. & Funakoshi, K. Wet subduction versus cold subduction. *Geophys. Res. Lett.* **32**, L13312 (2005).
33. Seton, M. et al. Global continental and ocean basin reconstructions since 200 Ma. *Earth Sci. Rev.* **113**, 212–270 (2012).
34. Leng, W. & Zhong, S. J. Controls on plume heat flux and plume excess temperature. *J. Geophys. Res. Solid Earth* **113**, B04408 (2008).
35. Turcotte, D. L. & Schubert, G. (eds) *Geodynamics* 3rd edn 192–193 (Cambridge Univ. Press, Cambridge, 2014).
36. Müller, R. D., Dutkiewicz, A., Seton, M. & Gaina, C. Seawater chemistry driven by supercontinent assembly, breakup, and dispersal. *Geology* **41**, 907–910 (2013).
37. Zhong, S. J. & Rudolph, M. L. On the temporal evolution of long-wavelength mantle structure of the Earth mantle since the Early Paleozoic. *Geochem. Geophys. Geosyst.* **16**, 1599–1615 (2015).
38. Hassan, R., Müller, R. D., Gurnis, M., Williams, S. E. & Flament, N. A rapid burst in hotspot motion through the interaction of tectonics and deep mantle flow. *Nature* **533**, 239–242 (2016).
39. Karato, S. I. *Deformation of Earth Materials: An Introduction to the Rheology of Solid Earth* (Cambridge Univ. Press, Cambridge, 2008).
40. Panasyuk, S. V. & Hager, B. H. A model of transformational superplasticity in the upper mantle. *Geophys. J. Int.* **133**, 741–755 (1998).
41. Čížková, H. & Bina, C. R. Effects of mantle and subduction-interface rheologies on slab stagnation and trench rollback. *Earth. Planet. Sci. Lett.* **379**, 95–103 (2013).
42. Nakakuki, T., Tagawa, M. & Iwase, Y. Dynamical mechanisms controlling formation and avalanche of a stagnant slab. *Phys. Earth Planet. Inter.* **183**, 309–320 (2010).
43. Bercovici, D. The generation of plate tectonics frommantle convection. *Earth. Planet. Sci. Lett.* **205**, 107–121 (2003).
44. Zhong, S. J. & Watts, A. B. Lithospheric deformation induced by loading of the Hawaiian Islands and its implications for mantle rheology. *J. Geophys. Res.* **118**, 6025–6048 (2013).
45. Kohlstedt, D. L. & Mackwell, S. J. in *Planetary Tectonics* (eds Waters, T. & Schultz, R.) 395–455 (Cambridge Univ. Press, New York, 2009).
46. Bunge, H. P. & Grand, S. P. Mesozoic plate-motion history below the northeast Pacific Ocean from seismic images of the subducted Farallon slab. *Nature* **405**, 337–340 (2000).
47. Liu, L., Spasojević, S. & Gurnis, M. Reconstructing Farallon plate subduction beneath North America back to the Late Cretaceous. *Science* **322**, 934–938 (2008).
48. Jolivet, L., Tamaki, K. & Fournier, M. Japan Sea, opening history and mechanism: a synthesis. *J. Geophys. Res.* **99**, 22237–22259 (1994).
49. Lee, C. & King, S. D. Dynamic buckling of subducting slabs reconciles geological and geophysical observations. *Earth. Planet. Sci. Lett.* **312**, 360–370 (2011).

Acknowledgements

We thank S. Goes and S. King for helpful comments on the manuscript. The work is supported by National Science Foundation through grant numbers 1135382, 1645245 and 1450181.

Author contributions

W.M. and S.J.Z. developed the concept of the project, designed models, developed the analysis methods and wrote the paper. W.M. performed the calculations.

Competing interests

The authors declare no competing interests.

Additional information

Supplementary information is available for this paper at https://doi.org/10.1038/s41561-018-0225-2.

Reprints and permissions information is available at www.nature.com/reprints.

Correspondence and requests for materials should be addressed to W.M. or S.Z.

Publisher's note: Springer Nature remains neutral with regard to jurisdictional claims in published maps and institutional affiliations.

Methods

Governing equations for thermal convection with phase changes. Our models of mantle convection are formulated in a 3D spherical shell geometry with the Boussinesq approximation and an infinitely large Prandtl number. The models include depth- and temperature-dependent viscosity, and the spinel–post-spinel phase change at 670 km depth. The governing equations are the conservation equations of the mass, momentum and energy, and the non-dimensional equations are[19,26,50]:

$$\nabla \cdot \mathbf{u} = 0 \tag{1}$$

$$-\nabla P + \nabla \cdot (\eta \dot{\varepsilon}) = \left(\mathrm{Ra} T - \sum_k \mathrm{Rb}^k \Gamma_k \right) \hat{\mathbf{e}}_r \tag{2}$$

$$\frac{\partial T}{\partial t} + (\mathbf{u} \cdot \nabla) T = \nabla^2 T + H \tag{3}$$

where $\mathbf{u}$ is velocity vector, P is the dynamic pressure, η is the viscosity, $\dot{\varepsilon}$ is the strain rate tensor, T is temperature, Γ_k is a phase change function for the kth phase change if multiple changes exist in the model, $\hat{\mathbf{e}}_r$ is the unit vector in radial direction, t is the time and H is the internal heat generation rate. Ra and Rb^k in equation (2) are the thermal Rayleigh number and phase-change Rayleigh number for the kth phase change, which are defined as:

$$\mathrm{Ra} = \frac{\rho g \alpha \Delta T R^3}{\kappa \eta_0} \tag{4}$$

$$\mathrm{Rb}^k = \frac{\Delta \rho_k g R^3}{\kappa \eta_0} \tag{5}$$

where ρ is the mantle reference density, g is the gravitational acceleration, α is the thermal expansivity at the surface, ΔT is the reference temperature difference between the surface and CMB, κ is the thermal diffusivity at the surface, η_0 is the reference viscosity, $\Delta \rho_k$ is the density jump for the kth phase change and R is the Earth's radius.

Mantle phase change and viscosity formulations. A phase-change function formulation is used here to represent phase changes as in earlier studies[19,26]. Γ_k is defined in dimensionless form as

$$\Gamma_k = \frac{1}{2}\left[1 + \tanh\left(\frac{\pi_k}{\delta}\right)\right] \tag{6}$$

where δ is the phase change width that measures the depth segment of phase change, and π_k is the dimensionless 'excess pressure' as

$$\pi_k = d - d_k - \gamma_k (T - T_k), \tag{7}$$

where d is the depth, d_k and T_k are the reference depth and temperature of phase change k, and γ_k is the Clapeyron slope. The Clapeyron slope is normalized by $\rho g R / \Delta T$.

In this study, we consider only the phase change at 670 km depth from the spinel to post-spinel phases (Supplementary Table 1). When Γ is smaller than 0.5, the spinel phase viscosity is applied even if it is below 670 km depth. When Γ is larger than 0.5, the post-spinel phase viscosity is applied. Previous geodynamic studies have demonstrated that the phase change dynamics is mainly controlled by γ and the density change of a phase change, whereas other phase change parameters are less important[19–21,26]. Experimental studies initially determined that γ for the spinel–post-spinel phase change was about $-3.0\,\mathrm{MPa\,K^{-1}}$, but more recent studies reported a much smaller magnitude of γ from $-0.4\,\mathrm{MPa\,K^{-1}}$ to $-2.0\,\mathrm{MPa\,K^{-1}}$ (see refs [30–32]). We consider different values of γ from 0 to $-3.5\,\mathrm{MPa\,K^{-1}}$ in our models.

Mantle viscosity in our models is both depth- and temperature-dependent and the non-dimensional form is

$$\eta(T, r) = \eta_r(r) \exp[E(0.5 - T)] \tag{8}$$

where $\eta_r(r)$ is the depth-dependent pre-factor and E is the non-dimensional activation energy. In our models, $\eta_r(r)$ is set such that a viscosity increase with depth by a factor of β occurs at the 670 km depth with β equal to 30, 100 and 300, which is broadly consistent with the geoid studies[7,8,51,52]. The lower mantle $\eta_r(r)$ is 2. Our models consider $E = 9.21$ (or $191\,\mathrm{KJ\,mol^{-1}}$, using parameters in Supplementary Table 1). Note that the dimensional viscosity depends on reference viscosity η_0 and hence Ra. Most of our models use $\mathrm{Ra} = 5 \times 10^7$ (Supplementary Table 1), which corresponds to a lower mantle viscosity of $\sim 2.5 \times 10^{22}$ Pa s (Supplementary Fig. 3b)—this values is generally consistent with post-glacial rebound studies[8].

For some cases, motivated by mineral physics and geoid modelling studies that suggest a significant viscosity reduction associated with the phase change[8,39,40], we also include a weak layer below the phase change boundary. This is defined using Γ. When $\Gamma < 0.5$, the mantle viscosity is the same as that in the transition zone. However, for $0.5 < \Gamma < 0.99$, the mantle is considered to be in a superplastic post-spinel phase, and its viscosity pre-factor is reduced to either the same as, or smaller than, that in the transition zone (Supplementary Table 2). The effective thickness of the viscosity reduction due to this weak layer is ~60 km depth. For $\Gamma > 0.99$, the normal post-spinel phase viscosity is applied. The resulting viscosity structure (Supplementary Fig. 3b) is similar to that in some geoid modelling studies[8].

Boundary and initial conditions and model resolution. We use a plate motion history model[33] as the time-dependent surface velocity boundary condition, while the CMB is free-slip. The models are computed for the past 130 Myr, because the slab structures are mainly controlled by plate motion history for approximately the past 130 Myr[6]. The plate motion history model provides realistic trench motions that may have important controls for slab structures[15–18,22,23]. The model of plate motion history put forward by Seton and colleagues[33] represents a synthesis of many previous plate motion reconstructions. The plate motion model has a different level of uncertainty for different time periods due to observational constraints, such that the plate motion model has a larger uncertainty for the more distant past. In general, plate motion history for the Cenozoic (the past 66 Myr) is well constrained[5,33]. As we have shown, the present-day slab structures, especially the stagnant slabs, are most sensitive to the Cenozoic plate motions (or more precisely, the past 20–30 Myr). Therefore, we judge that the plate motion history model[33] used here is adequate for our studies, although it would be desirable to test the effects of different plate motion history models.

The surface temperature is prescribed as a constant 0, whereas the CMB has a thermally insulating boundary condition. The insulating CMB prevents thermal upwelling plumes from being generated, so our models can focus on the evolution of subducted slabs. The initial mantle temperature below the lithosphere (that is, below the 150 km depth) is 0.52 (or 1,300 °C) everywhere including the CMB (that is, no bottom thermal boundary layer). The initial temperature in oceanic lithosphere is calculated from a plate model[35] based on lithospheric ages at 130 Ma[36]. The initial non-dimensional temperature for continental lithosphere increases linearly from 0 at the surface to 0.52 (that is, the mantle interior temperature) at 150 km depth (Supplementary Fig. 3a shows horizontally averaged temperature versus depth for the present day, which is similar to the initial temperature).

Governing equations (1)–(3) with the initial and boundary conditions are solved using CitcomS[50,53] on parallel computers Yellowstone and Cheyenne operated by NCAR. For most cases, we use a mesh with $12 \times 128 \times 128 \times 80$ grids and employ grid refinements near surface and phase transition depths in radial direction. With this grid, the models have a horizontal resolution of ~50 km at the surface and ~30 km near the CMB. For Case 4HR, we use a mesh with $12 \times 256 \times 256 \times 104$ which gives horizontal resolutions of approximately 25 km and 15 km at the surface and CMB, respectively.

Quantifying trench motion. We quantify time-dependent trench motions at different subduction zones using the following scheme. We first calculate the divergence of the surface velocity field at different time points to determine plate convergent/divergent boundaries[54]. At a given time point along the cross-section of each subduction zone, we determine the location of the maximum amplitude of the divergence and assign this location to be the trench location. From this time-dependent trench location, we then calculate the averaged trench location over a 3 Myr time window. We can calculate the trench motion based on the time-smoothed trench location at each subduction zone. The results for the northern Honshu, northern Mariana and North America subduction zones are given in Fig. 3a. Note that the Mariana trench did not exist until ~50 Ma, so its trench motion is computed for the past 50 Myr. Another scheme to determine the trench motion could be devised directly from the plate motion model, but we find that by working with a scalar (that is, divergence) this post-processing procedure is efficient. We also determine the age of subducting lithosphere at the trench for different subduction zones (Fig. 3b) using Gplates (www.gplates.org) and age data from ref. [36].

Code availability. The mantle convection code CitcomS is available at www.geodynamics.org/cig/software/citcoms/. The GMT code used to make the figures is available at www.soest.hawaii.edu/gmt/.

Data availability

All of the materials of this study are available on request from the corresponding authors. The S-wave tomography model S40RTS of ref. [9] is available at http://jritsema.earth.lsa.umich.edu//Research.html. The S-wave tomography model SEMUCB_WM1 of ref. [10] is available at http://seismo.berkeley.edu/wiki_br/Main_Page. The P-wave tomography model GAP_P4 of ref. [12] is available at www.godac.jamstec.go.jp/catalog/data_catalog/metadataDisp/GAP_P4?lang=en.

The temperature anomalies for Case 4 at present day and the related data are available at https://doi.org/10.6084/m9.figshare.6916256.v1.

References

50. Zhong, S. J., McNamara, A., Tan, E., Moresi, L. & Gurnis, M. A benchmark study on mantle convection in a 3-D spherical shell using CitcomS. *Geochem. Geophys. Geosyst.* **9**, Q10017 (2008).
51. King, S. D. Radial models of mantle viscosity: results from a genetic algorithm. *Geophys. J. Int.* **122**, 725–734 (1995).
52. Rudolph, M. L., Lekić, V. & Lithgow-Bertelloni, C. Viscosity jump in Earth's mid-mantle. *Science* **350**, 1349–1352 (2015).
53. Zhong, S. J., Zuber, M. T., Moresi, L. & Gurnis, M. Role of temperature-dependent viscosity and surface plates in spherical shell models of mantle convection. *J. Geophys. Res. Solid Earth* **105**, 11063–11082 (2000).
54. Li, M. et al. Quantifying melt production and degassing rate at mid-ocean ridges from global mantle convection models with plate motion history. *Geochem. Geophys. Geosyst.* **17**, 2884–2904 (2016).

nature geoscience

SUPPLEMENTARY INFORMATION

https://doi.org/10.1038/s41561-018-0225-2

In the format provided by the authors and unedited.

Slab stagnation due to a reduced viscosity layer beneath the mantle transition zone

Wei Mao* and Shijie Zhong*

Department of Physics, University of Colorado, Boulder, CO, USA. *e-mail: wei.mao@colorado.edu; szhong@colorado.edu

Supplementary discussion. Slab structures from three different seismic models

We compare slab structures (i.e., seismically fast anomalies) from three seismic tomography models: P-wave velocity model GAP_P4[12], S-wave velocity models SEMUCB_WM1[10] and S40RTS[9]. The general slab structures are remarkably similar for these three seismic models, although important differences exist especially around 670 km depth (Supplementary Fig. S1 and S2). The common features from three models include: 1) slabs penetrate into the lower mantle in Americas, Tethys, eastern Asia, Tonga and western Java, and some of them even reach CMB, as shown in most previous seismic tomography models[1-3]; 2) horizontally deflected slabs near the 670 km depth in the northern Honshu, northern Mariana, Tonga, Calabria, northern Chile, and western Java subduction zones.

However, the depths at which some slabs reach may differ among these three seismic models. For example, in the northern Mariana cross-section, slabs from model GAP_P4 penetrate through 670 km depth and just reach above ~1000 km depth at the eastern side of the profile (Supplementary Fig. 2r), but models SEMUCB_WM1 and S40RTS do not show significant slab penetration below the 670 km depth (Supplementary Fig. 2b and 2j). In the Tonga subduction zone, slabs from models SEMUCB_WM1 and S40RTS are bottomed at ~1000 km depth (Supplementary Fig. 2e and 2m), but model GAP_P4 shows significant slabs below 1000 km depth (Supplementary Fig. 2u). In the northern Chile, although slabs from model GAP_P4 are stagnant above 670 km depth (Supplementary Fig. 2v), slabs from model SEMUCB_WM1 are stagnant above 1000 km depth (Supplementary Fig. 2f) and slabs from S40RTS seep through 1000 km depth into the deep lower mantle (Supplementary Fig. 2n). In Calabria, while the slabs from GAP_P4 appear to flatten mainly at ~670 km depth (Supplementary Fig. 2w), the slabs from SEMUCB_WM1 and S40RTS clearly seep through the 670 km depth to below 1200 km depth (Supplementary Fig. 2g and 2o). The differences in the depths that the slabs reach from these three models suggest that caution should be exercised in interpreting slab stagnation at 1000 km depth[12], as also suggested in ref 15. Thus, in this study we mainly focus on the common slab features shown by all these seismic tomography models.

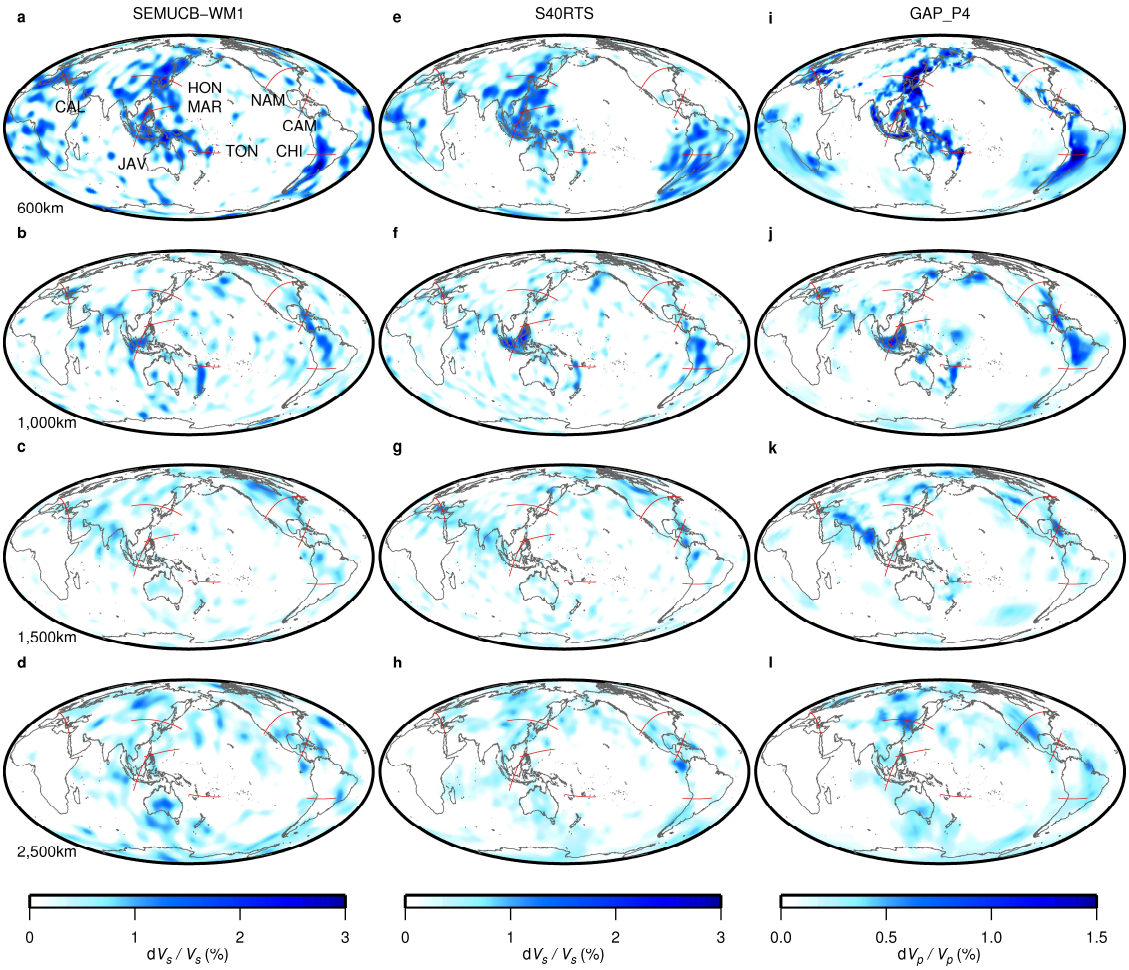

Supplementary Figure 1: **Map view of three different seismic tomography models.** The four rows are for 600 km, 1000 km, 1500 km and 2500 km depth, respectively, and only seismically fast anomalies are displayed to highlight slab structures. Panels **a-d** and **e-h** are for S-wave velocity anomalies from seismic model SEMUCB_WM1[10] and S40RTS[9], respectively. Panels **i-l** are for P-wave velocity anomalies from seismic model GAP_P4[12]. In each figure, the eight red lines represent eight cross sections used in Supplementary Figure 2 (CAL for Calabria, JAV for western Java, HON for northern Honshu, MAR for northern Mariana, TON for Tonga, NAM for North America, CAM for Central America, and CHI for northern Chile). Note that except for Calabria and North America, the other cross sections are identical to that used in ref. 12. The general slab structures are remarkably similar for these three seismic models, although important differences exist especially in the transition zone (i.e., 600 km depth maps), which is discussed in more details in Supplementary discussion.

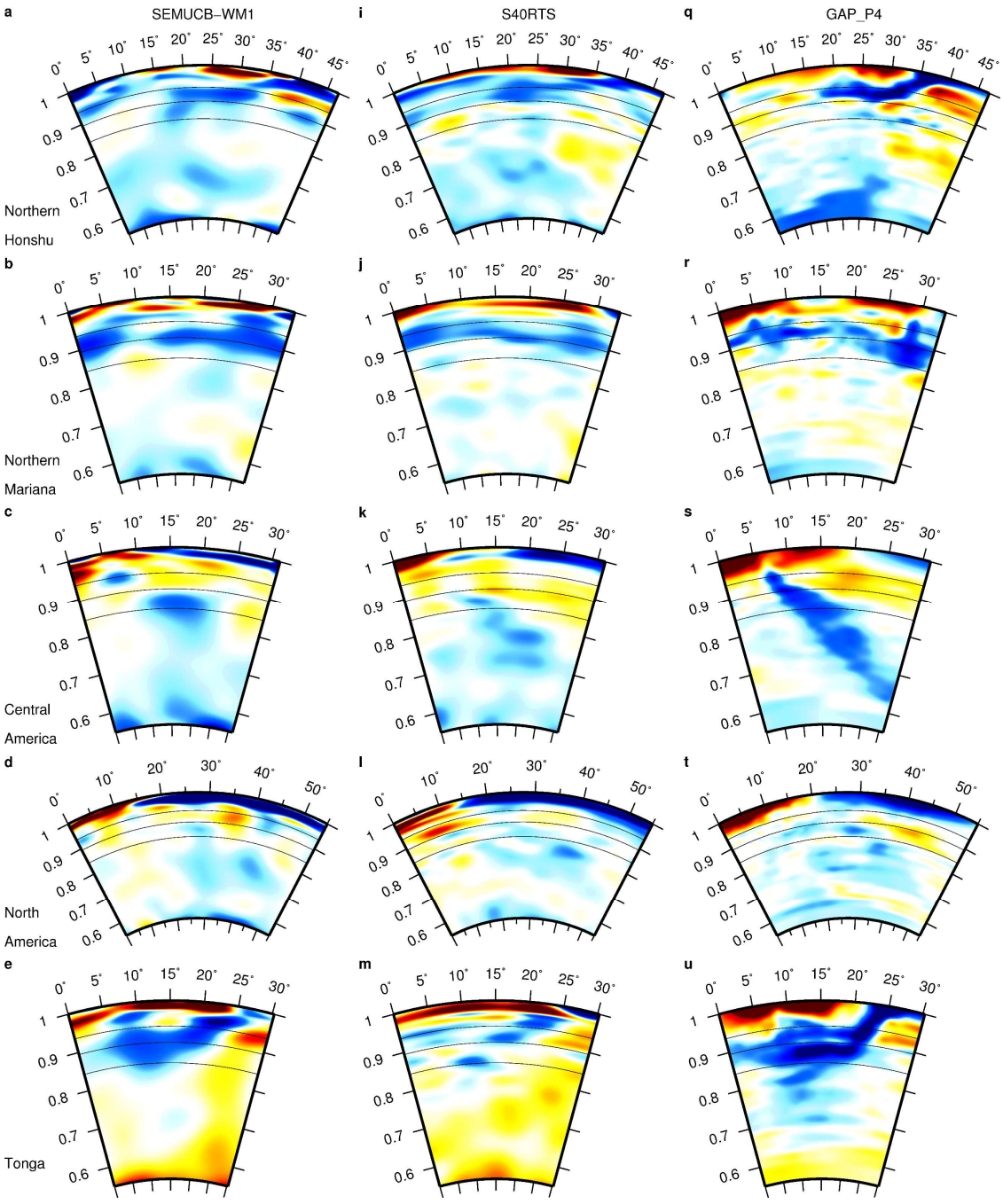
a
SEMUCB–WM1
i
S40RTS
q
GAP_P4
Northern Honshu
b
j
r
Northern Mariana
c
k
s
Central America
d
l
t
North America
e
m
u
Tonga

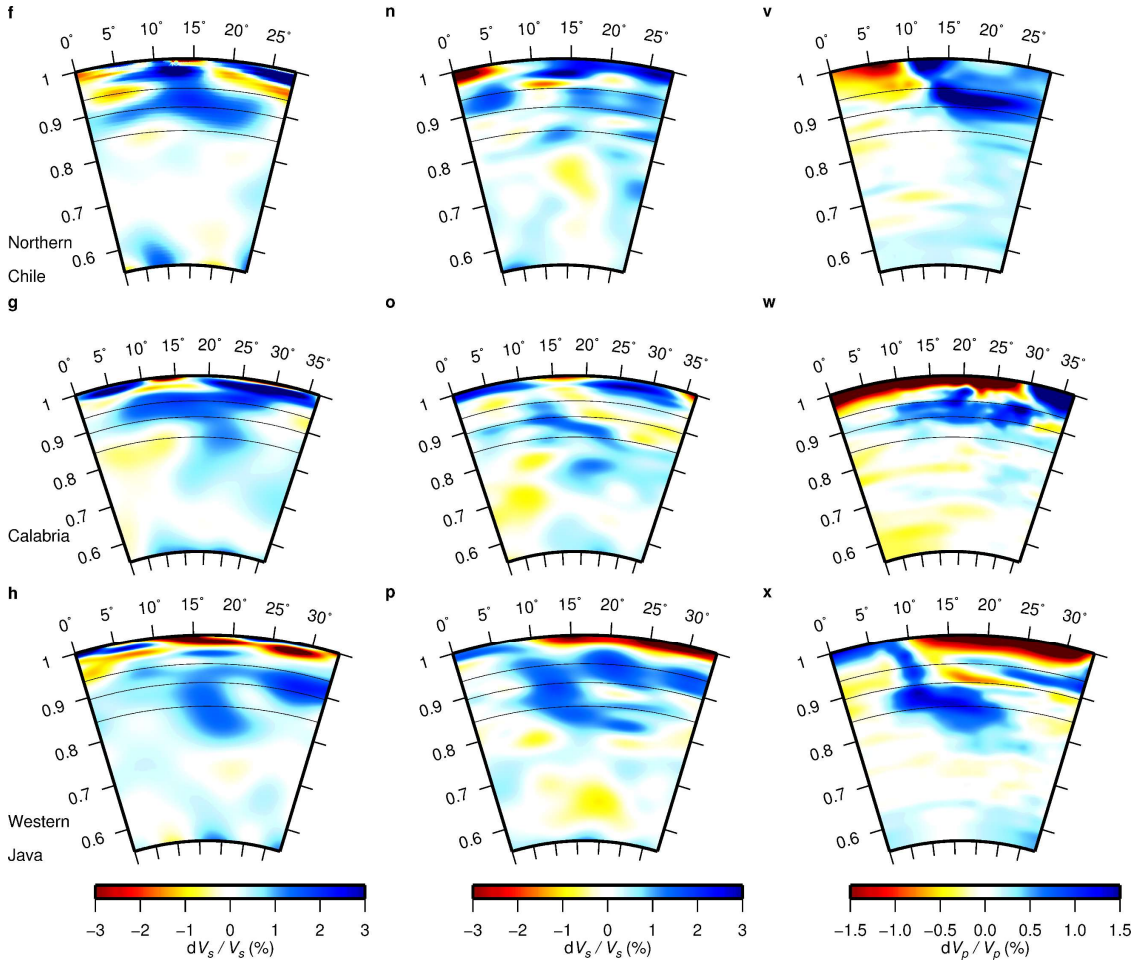

Supplementary Figure 2: **Cross-sectional view of three different seismic tomography models.** The eight rows are for the northern Honshu, northern Mariana, Central America, North America, Tonga, northern Chile, Calabria and western Java, respectively. Panels **a-h** (the first column) and **i-p** (the second column) are for S-wave velocity anomalies from seismic model SEMUCB_WM1[10] and S40RTS[9], respectively. Panels **q-x** (the third column) are for P-wave velocity anomalies from seismic model GAP_P4[12]. See Supplementary discussion on comparison of seismic models.

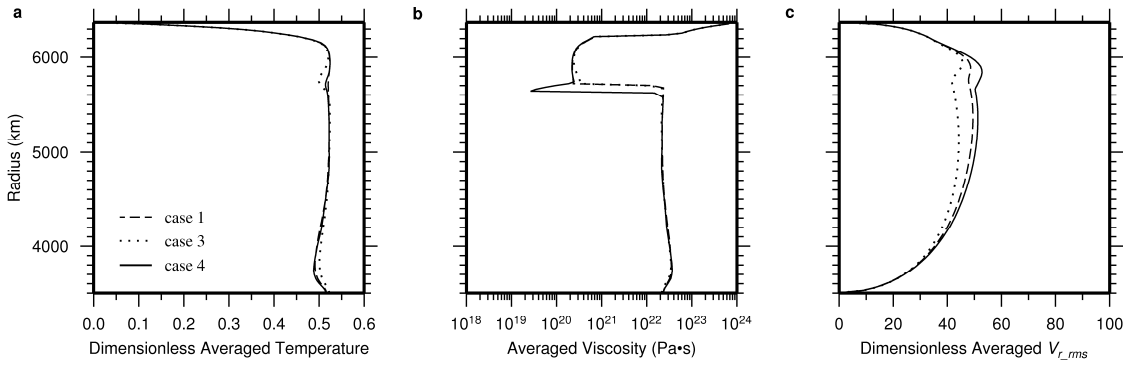

Supplementary Figure 3: **Present-day model horizontal averaged parameter values. a-c** are the dimensionless horizontally averaged temperature, the dimensional horizontally averaged viscosity and the dimensionless horizontally averaged root-mean-square radial velocity V_{r_rms} for Case 1 (dashed curve), Case 3 (dotted curve) and Case 4 (solid curve), respectively. Both the horizontally averaged temperature and V_{r_rms} decrease significantly in the transition zone for Cases 3 and 4 due to slab stagnation, but not for Case 1 with no phase transition.

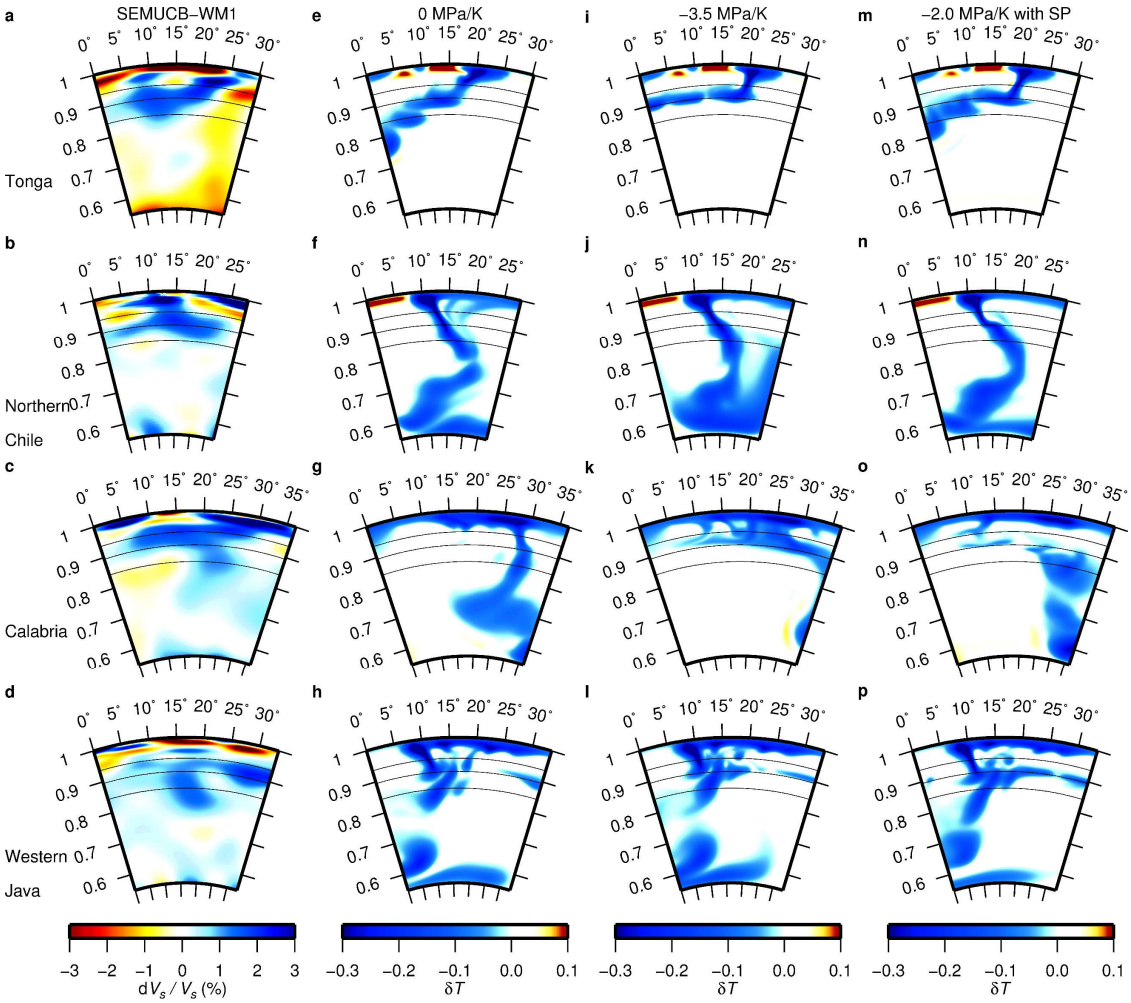

Supplementary Figure 4: **Cross-sectional view of seismic anomalies and present-day model temperature anomalies for different subduction zones for Cases 1, 3 and 4 (additional to those profiles in Fig. 2).** Note that for the Central America and Northern Chile, seismic models S40RTS[9] and GAP_P4[12] show more clearly continuous slab structures throughout the mantle (Supplementary Fig. 2k, 2s, 2n, and 2v) that agree better with the convection models (Fig. 2). The four rows are at for Tonga, northern Chile, Calabria and western Java subduction zones, respectively. Panels **a-d** are for S-wave velocity anomalies at these four subduction zones from model SEMUCB_WM1[10]. Panels **e-h**, **i-l** and **m-p** are model dimensionless temperature anomalies for these four subduction zones for Cases 1, 3 and 4, respectively. Our best fit model, Case 4, also reproduces the confined slab above 1000 km depth at Tonga. Case 4 also reproduces the slab stagnation in the transition zone and lower mantle slabs at Calabria and western Java as seen in the seismic models. At northern Chile, all of our models produce slabs that directly extend to the CMB with no stagnant slabs in the transition zone. While the model slab structure at northern Chile differs from that in SEMUCB-WM1, it seems that seismic models also differ significantly among themselves here (Supplementary Fig. 2f, 2n, and 2v) with

S40RTS and GAP_P4 both showing prominent slab structure in the lower mantle, similar to the convection models.

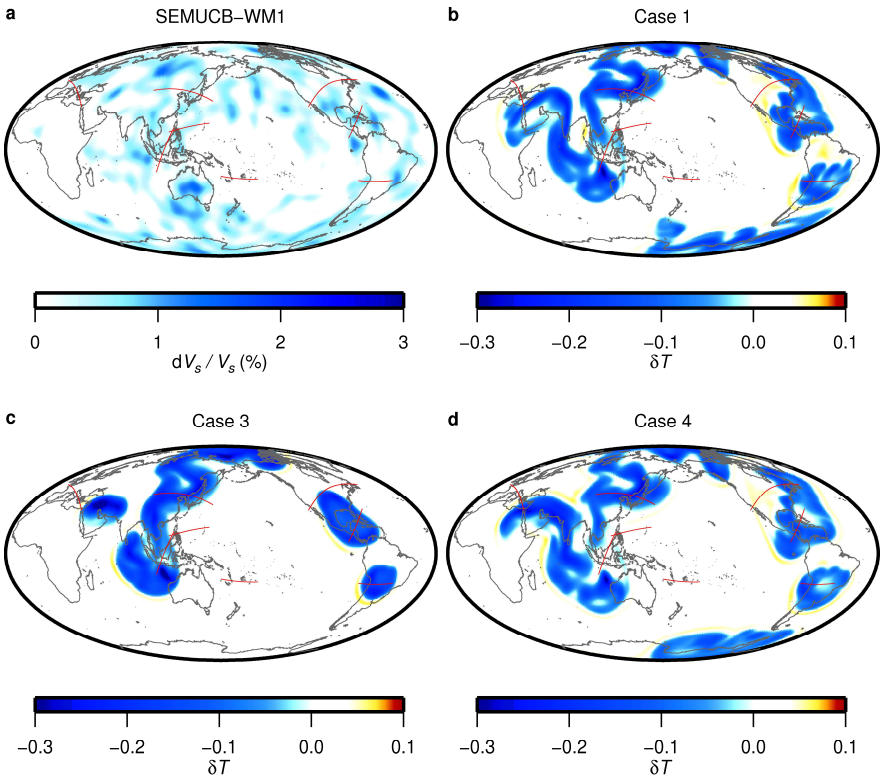

Supplementary Figure 5: **Map view of seismic anomalies and present-day model temperature anomalies at 2500 km depth.** Panel a is for the seismic model SEMUCB_WM1, and panels b-d are for Cases 1, 3 and 4, respectively**.** The general slab structures at 2500 km depth are similar for the seismic model and Cases 1 and 4, but Case 3 with a large amplitude of Clapeyron slope (-3.5 MPa/K) does not have any slabs in the lower mantle including at 2500 km depth beneath Antarctica and the southern Pacific. Note that similar comparisons for SEMUCB_WM1, and Cases 1, 3 and 4 at other depths (600 km, 1000 km, and 1500 km) can be found in Fig. 1.

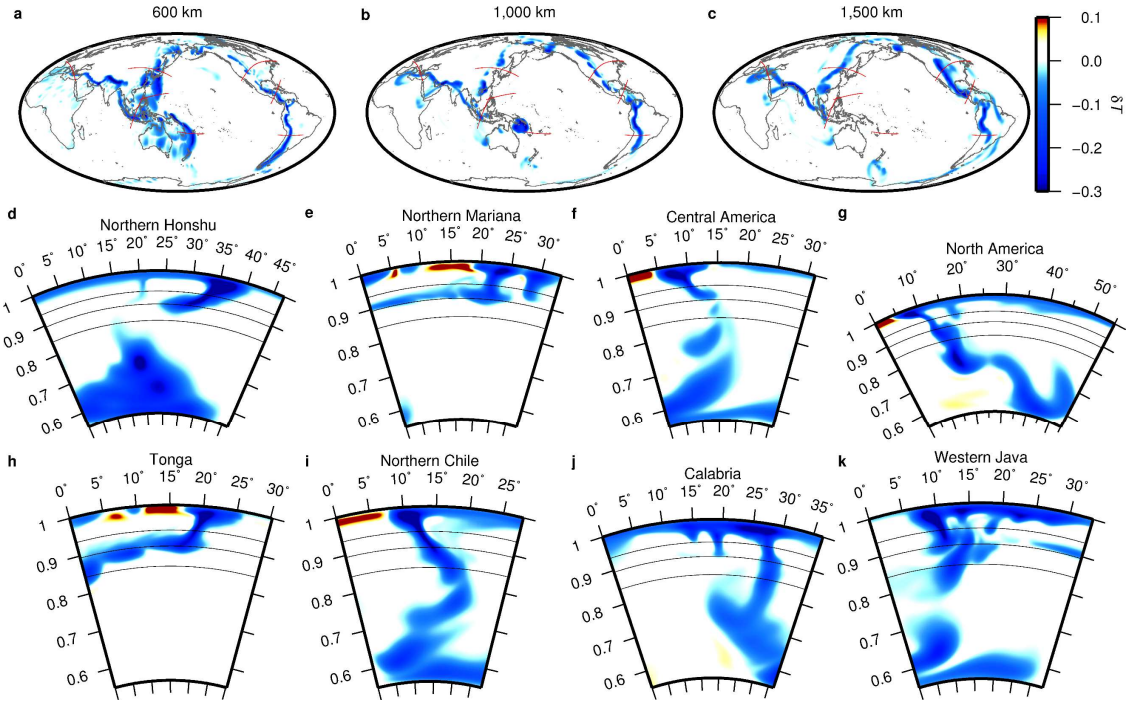

Supplementary Figure 6: **Map and cross-sectional view of present-day model temperature anomalies of Case 2.** Panels **a-c** are model dimensionless temperature anomalies for Case 2 at 600, 1000 and 1500 km depth, respectively. Panels **d-k** are model dimensionless temperature anomalies for Case 2 at the eight subduction zones. The results of Case 2 with Clapeyron slope of -2.0 MPa/K are generally similar to that of Case 1 without the phase change (Fig. 1d-1f, Fig. 2e-h and Supplementary Fig. 4e-h).

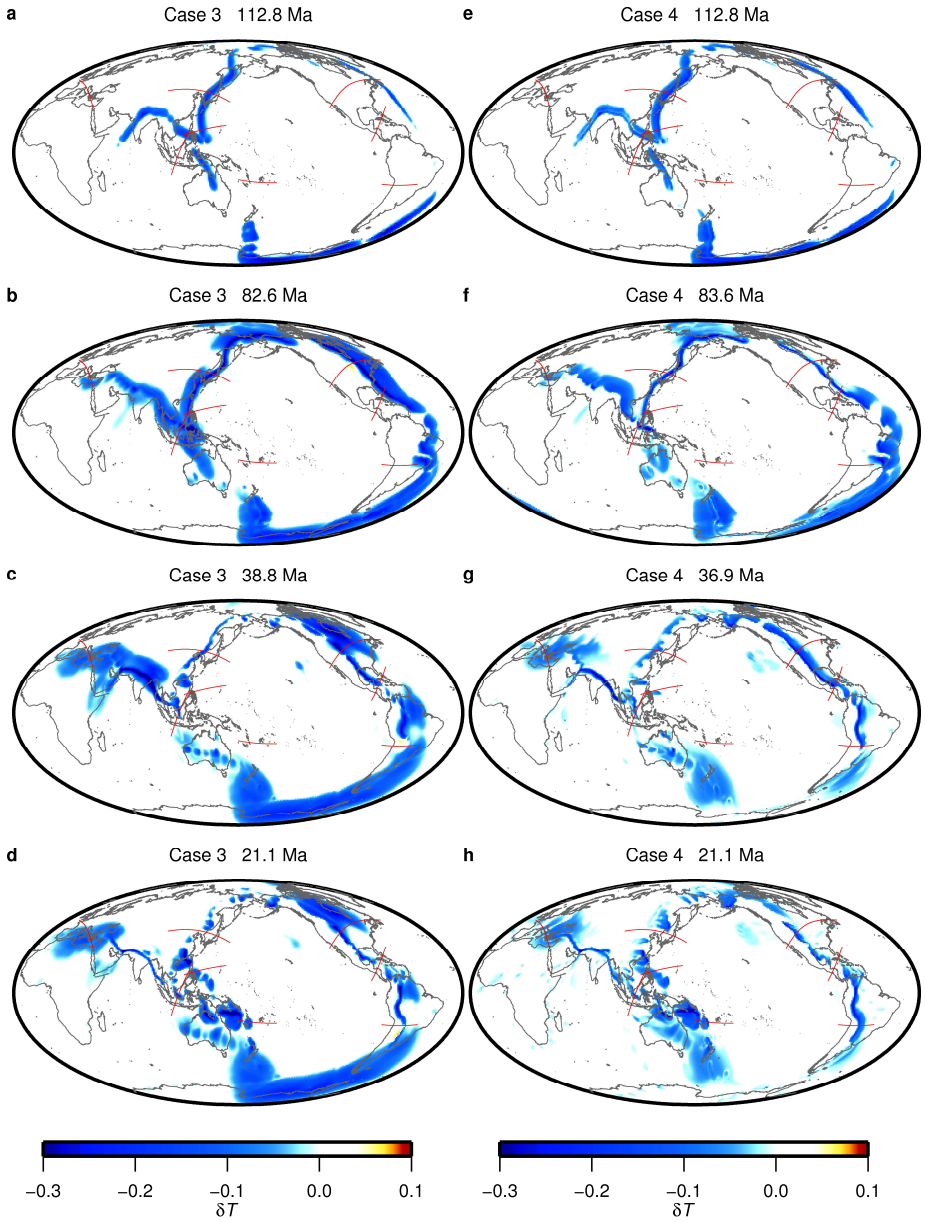

Supplementary Figure 7: **Map view of model temperature anomalies of Cases 3 and 4 at 600 km depth and at different times.** Panels **a-d** are model dimensionless temperature anomalies at 600 km depth for Case 3 at 112.8, 82.6, 38.8 and 21.1 Ma, respectively. Panels **e-h** are model temperature anomalies at 600 km depth for Case 4 at 112.8, 83.6, 36.9 and 21.1 Ma, respectively. Note that the corresponding present-day temperature anomalies for Cases 3 and 4 can be seen in Figures 1g and 1j, respectively. We would like to make two remarks. 1) The present-day model stagnant slabs in the southern Pacific and Antarctica from Case 3 (Fig. 1g) result from subduction between 120-100 Ma near Antarctica, but have never made to the lower mantle (Fig. 1h-1i, Supplementary Figure 5c, 7a-d). 2) Significant present-day stagnant slabs in Japan and Mariana subduction zones in Case 4 came from subduction in the last 20 Myr (Fig. 1j and Supplementary Figure 7h).

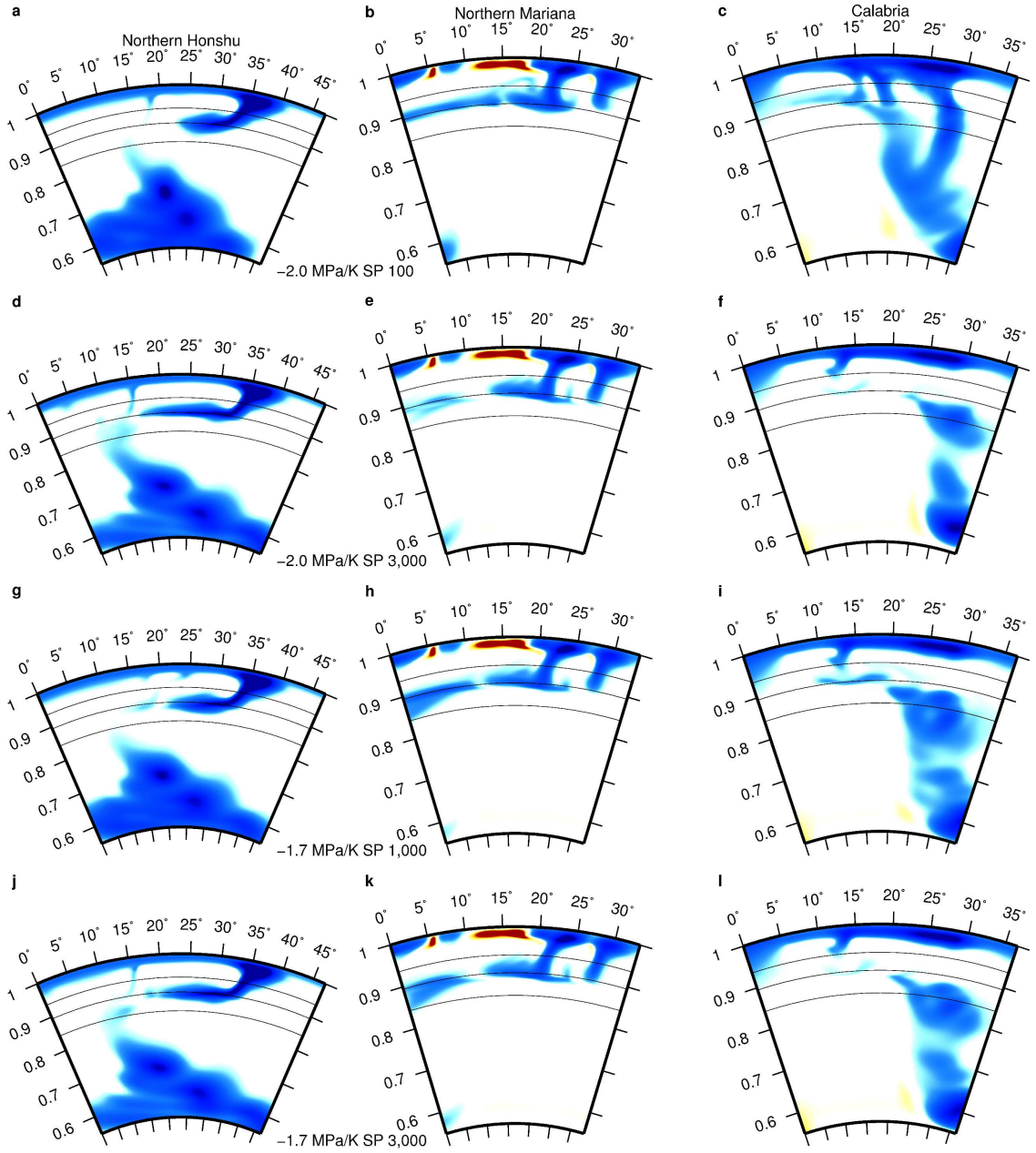

Supplementary Figure 8: **Cross-sectional view of present-day model temperature anomalies of different weak layer viscosity models.** Panels **a-c**, **d-f**, **g-i** and **j-l** are model dimensionless temperature anomalies for Cases 5, 6, 7 and 8 (Supplementary Table 2) at the northern Honshu, northern Mariana and Calabria, respectively. These three subduction zones are shown, because they provide the best comparison among these four cases and Case 4. Case 5 produces slabs that are similar to Case 2 that does not have any weak layer (Supplementary Fig. 6). Case 6 produces a longer stagnant slab in the northern Honshu (panel d) than Case 4 (Fig. 2m), but less stagnant slabs are produced in the Mariana and

Calabria (panels e and f) than in Case 4 (Fig. 2n and Supplementary Fig. 4o). Case 7 with γ=-1.7 MPa/K produces slab structures that are quite similar to those in Case 4 with γ=-2 MPa/K, except that the stagnant slab in the Honshu is slightly shorter (panel g). For Case 8 with further reduced viscosity in the weak layer, the stagnant slab in the Honshu is longer than Case 7 (panels j and g), although the stagnant slabs in other subduction zones are reduced (panel l). These cases suggest that our slab structure results for Case 4 are generally applicable to Clapeyron slopes between -2.0 and -1.7 MPa/K, and that the weak layer below the phase change needs to be ~10 weaker than the transition zone to be effective.

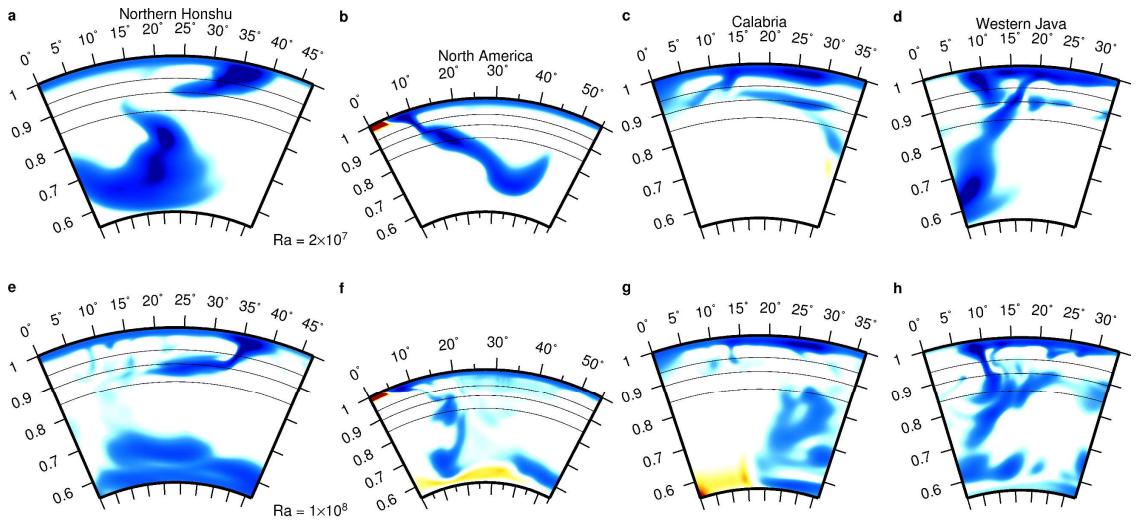

Supplementary Figure 9: **Cross-sectional view of present-day model temperature anomalies of different Ra models.** Panels **a-d** and **e-h** are model dimensionless temperature anomalies for Cases 9 ($Ra=2\times10^7$) and 10 ($Ra=10^8$) at the northern Honshu, North America, Calabria and western Java, respectively. These four subduction zones are shown, because they provide the best comparison among these cases and Case 4.

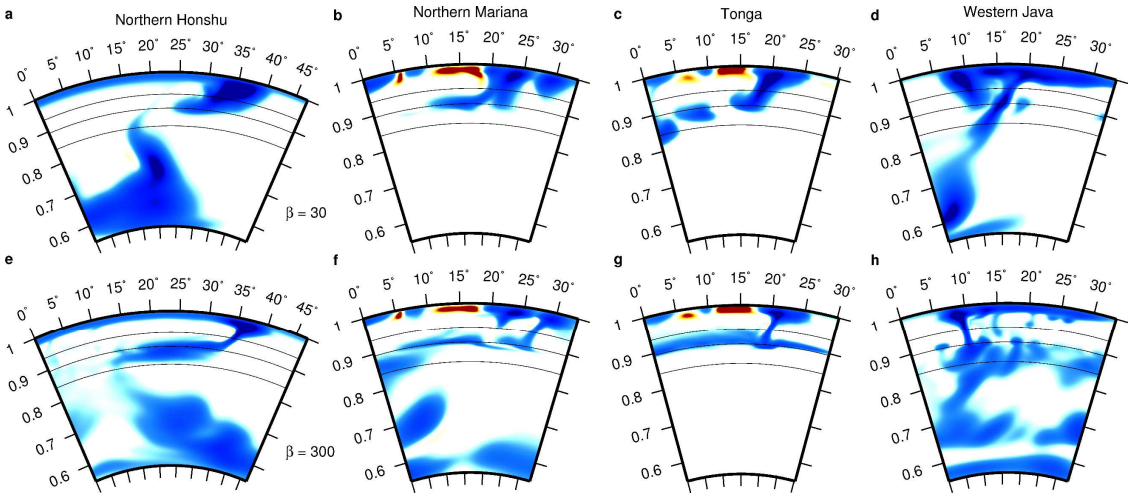

Supplementary Figure 10: **Cross-sectional view of present-day model temperature anomalies from models with different viscosity contrast β between the upper and lower mantles.** Panels **a-d** and **e-h** are model dimensionless temperature anomalies for Cases 11 (β=30) and 12 (β=300) at the northern Honshu, northern Mariana, Tonga and western Java, respectively. These four subduction zones are shown, because they provide the best comparison among these cases and Case 4. Note that we vary β by only changing the upper mantle viscosity while keeping the lower mantle viscosity the same.

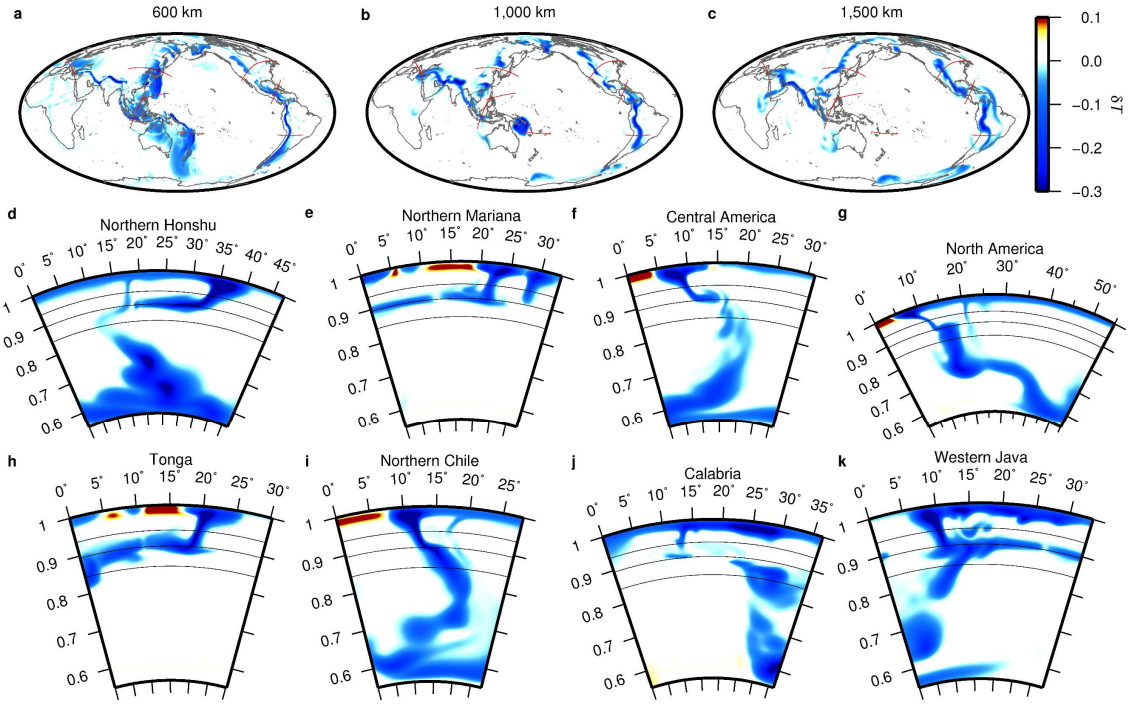

Supplementary Figure 11: **Map and cross-sectional view of present-day model temperature anomalies of Case 4HR.** Panels **a-c** are model dimensionless temperature anomalies at 600, 1000 and 1500 km depth, respectively. Panels **d-k** are model dimensionless temperature anomalies at the eight subduction zones. Case 4HR is identical to Case 4 except that the grid resolution is increased from 12×128×128×80 to 12×256×256×104 (i.e., ~25 km and ~15 km horizontal resolution at the surface and CMB, respectively). The results of Case 4HR are the same as Case 4 except for minor differences, such as the lithospheric drip to the left side of stagnant slab at the northern Honshu. This resolution test verifies the robustness of our model results.

Supplementary Table S1: **Model parameters**

Parameters	Value
Earth's radius, R	6370 km
Mantle thickness, h	2870 km
Mantle density, ρ	3300 kg/m^3
Gravitational acceleration, g	9.8 m/s^2
Thermal expansivity, α[a]	3×10^{-5} /K
Reference temperature difference, ΔT	2500 K
Thermal diffusivity, κ[a]	10^{-6} m^2/s
Gas constant, R_{gas}	8.314 J/(K·mol)
Spinel to post-spinel density change, $\Delta\rho_1/\rho$	8%
Spinel to post-spinel phase change width, δ_1	40 km
Spinel to post-spinel phase change reference depth, d_1	670 km
Spinel to post-spinel phase change reference temperature, T_1	1573 K

[a]Thermal expansivity decreases by a factor of 2.5 from surface to the CMB, while thermal diffusivity increases by a factor of 2.18 from surface to the CMB.

Supplementary Table S2: **Input parameters for different models**[a]

Model	β	γ (MPa/K)	*Ra*	SP-Reduction
1	100	0	5×10^7	1
2	100	-2.0	5×10^7	1
3	100	-3.5	5×10^7	1
4	100	-2.0	5×10^7	1000
4HR[b]	100	-2.0	5×10^7	1000
5	100	-2.0	5×10^7	100
6	100	-2.0	5×10^7	3000
7	100	-1.7	5×10^7	1000
8	100	-1.7	5×10^7	3000
9	100	-2.0	2×10^7	1000
10	100	-2.0	10^8	1000
11	30	-2.0	5×10^7	1000
12	300	-2.0	5×10^7	1000

[a]*β*, *γ*, *Ra*, and *SP-Reduction* represent viscosity increase at the 670 km depth, Clapeyron slope (in MPa/K), Rayleigh number, and properties of the weak layer below the phase boundary, respectively. The value for SP-Reduction represents the factor of viscosity reduction for the weak layer. When it is 1, no weak layer is present.

[b]Case 4HR is identical to Case 4 except that the grid resolution is increased from 12×128×128×80 to 12×256×256×104 (i.e., ~25 km and ~15 km horizontal resolution at the surface and CMB, respectively).